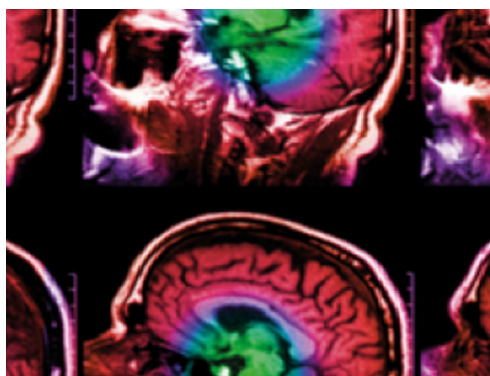


PAPER

Radiation dose reduction and static image quality assessment using a channelized hotelling observer on an angiography system upgraded with clarity IQ

To cite this article: O Ortenzia *et al* 2020 *Biomed. Phys. Eng. Express* **6** 025008

View the [article online](#) for updates and enhancements.



IPEM | IOP

Series in Physics and Engineering in Medicine and Biology

Your publishing choice in medical physics,
biomedical engineering and related subjects.

Start exploring the collection—download the
first chapter of every title for free.

Biomedical Physics & Engineering Express



PAPER

Radiation dose reduction and static image quality assessment using a channelized hotelling observer on an angiography system upgraded with clarity IQ

RECEIVED
26 November 2019

REVISED
20 January 2020

ACCEPTED FOR PUBLICATION
7 February 2020

PUBLISHED
18 February 2020

O Ortenzia¹ , V Trojani^{2,3}, M Bertolini² , A Nitrosi², M Iori² and C Ghetti¹

¹ Servizio di Fisica Sanitaria, Azienda Ospedaliera Universitaria di Parma, Parma, Italy

² Servizio di Fisica Medica, Azienda USL-IRCCS di Reggio Emilia, Reggio Emilia, Italy

³ Scuola di Specializzazione Fisica Sanitaria, Università degli Studi di Bologna, Bologna, Italy

E-mail: oortenzia@ao.pr.it

Keywords: x-ray angiography, channelized hotelling observer model, image quality, noise reduction technology, radiation dose

Abstract

The goal of this paper was the comparison of radiation dose and imaging quality before and after the Clarity IQ technology installation in a Philips AlluraXper FD20/20 angiography system using a Channelized Hotelling Observer model (CHO). The core characteristics of the Allura Clarity IQ technology are its real-time noise reduction algorithms (NRT) combined with state-of-the-art hardware; this technology allows to implement acquisition protocols able to significantly reduce patient entrance dose. To measure the system performances in terms of image quality we used a contrast detail phantom in a clinical scatter condition. A Leeds TO10 phantom has been imaged between two 10 cm thick homogeneous solid water slabs. Fluoroscopy images were acquired using a cerebral protocol at 3 dose levels (low, medium and high) with a field-of-view (FOV) of 31 cm. Cineangiography images were acquired using a cerebral protocol at 2 fps. Thus, 4 acquisitions were obtained for the conventional technology and 4 acquisitions were taken after the Clarity IQ upgrade, for a total of 8 different image sets. A validated 40 Gabor channels CHO with an internal noise model compared the image sets. Human observers' studies were carried out to tune the internal noise parameter. We showed that the CHO did not detect any significant difference between any of the image sets acquired using the two technologies. Consequently, this x-ray imaging technology provides a non-inferior image quality with an average patient dose reduction of 57% and 28% respectively in cineangiography and fluoroscopy. The Clarity IQ installation has certainly allowed a considerable improvement in patient and staff safety, while maintaining the same image quality.

1. Introduction

In recent years new NRT algorithms have been introduced and applied in clinical practice to reduce patient and staff exposure in interventional radiology procedures without degrading the image quality.

Radiation dose decreasing can be easily monitored after the introduction of a new technology, on the contrary, image quality (IQ) evaluation is a critical step during the optimization process of any medical imaging system or image-processing algorithm [1]. Different methods have been proposed to evaluate image quality performance of flat-panel angiography equipment.

Traditional spatial-domain metrics, such as contrast, noise, contrast-to-noise ratio (CNR) and spatial resolution, although very intuitive, cannot provide an overall description of a system performance.

Computing spatial frequency domain evaluations, such as modulation transfer function (MTF) and noise power spectrum (NPS) can provide a comprehensive metric through the use of noise equivalent quanta (NEQ of an image) and detective quantum efficiency (DQE of a system). However, these measurements require unprocessed or 'raw' image data and they do not consider some important effects like scattered radiation, antiscatter grid, magnification and focal blurring [2].

Observer models based on statistical decision theory have been introduced to overcome the limitations of these commonly used spatial-domain and spatial frequency-domain measurements. They are not to be intended as an alternative to the traditional physical characterization; instead, they offer complementary information about the system or the reconstruction algorithm.

In diagnostic medical imaging, the human observer is the principal agent of the decision-making process. Therefore, it is now widely accepted that image quality should be evaluated using task-based criteria to model, for example, the human observer performance in a lesion-detection task [3]. To include the human observers contribution into the image quality evaluation, psychophysical studies to assess their performance are compulsory. However, they are costly and time-consuming. Hence, numerical observer algorithms that predict and simulate human observer behaviour, are being employed as a surrogate approach for image quality assessment.

Among the different kinds of models found in literature, the CHO is widely used due to its potential; in fact, it has been shown in several studies that the CHO produces detection performances that correlate well with those of human observers.

However, in some cases, the CHO outperforms humans [4–9]: to solve this issue, it is common to introduce an internal noise model within the CHO. Internal noise represents a real phenomena occurring in the human visual system, i.e. variations in neural firing, intrinsic inconsistency in receptor response and a loss of information during neural transmission [10, 11]. The use of an internal-noise model has been proven successful in different works [12, 13]. To validate the model observer a specific parameter has to be chosen empirically based on the performance of available human observers. The tuning of said parameter is done by training the model to improve predictions using a set of labeled training data; thus, this model training can be classified as a supervised-learning.

Our aim was to evaluate how much the NRT has reduced the radiation dose in typical neuro interventional procedures and the effect on imaging quality using a previously validated 40 Gabor channels CHO model with internal noise [13].

2. Methods

The images used in this study were acquired in two steps. In the first one, data collection was carried out on Allura Xper FD20/20 angiography system manufactured by Philips Healthcare (Best, The Netherlands) equipped with standard image processing and exposure system settings. Subsequently, in the second phase, we repeated all the acquisitions on the same system (identical geometry set-up) upgraded with the advanced image processing and optimised exposure

system settings to enable patient dose reduction (Clarity IQ; Philips Healthcare, Best, the Netherlands). From now on, these configurations will be respectively designated as 'Xper' and 'Clarity IQ'.

The angiography system FD20/20 used for this study is dedicated to neurointerventional procedures, it combines two dynamic flat-panel detectors on both the frontal and the lateral plane (nominal maximum FOVs: $30 \times 38 \text{ cm}^2$ and $30 \times 30 \text{ cm}^2$). The two detection systems are equivalent. The CsI(Tl) detectors (PX4700HS) are coupled with an a-Si matrix with a nominal pixel pitch of 0.154 mm, manufactured by Trixell (Moirans, France).

2.1. Imaging technology

Philips AlluraClarity (commercially named Clarity IQ) is a FDA approved imaging technology used to reduce image noise in angiography systems and it was commercially introduced outside the US in mid-2012. The most important characteristic of this tool is the combination of advanced real-time NRT algorithms with state-of-the-art hardware; this technology allows to implement acquisition protocols able to significantly reduce patient entrance dose. The algorithm was engineered using anatomy-specific optimization of the full acquisition chain, taking into account the typical exposure parameters (e.g., beam filtering, spot size, pulse width, grid switch), the detector technology and the image processing [14]. The great advantage of this technology is the potential individual optimization of every clinical task. Noise reduction performed by this technology affects both temporal and spatial noise. Temporal noise reduction refers to the processing performed over time and thus, across subsequent images. Spatial noise reduction refers to the processing performed over different regions within a single image [15]. Temporal noise is reduced by averaging several frames. The Clarity IQ algorithm uses motion compensation by aligning moving structures before applying an averaging process [16].

Spatial noise reduction finds the noise within a single image and filters it out pixel by pixel. Pixels within a neighborhood are taken into account for the spatial filtering algorithms. Consequently, image noise is filtered averaging the pixel intensity.

In order to prevent information loss, NRT finds the predominant signal structures on the image. These structures are excluded from the low-pass spatial filtering performed in the second step. Afterwards, only the parts of the image considered featureless are smoothed.

This imaging technology is matched with an added beam filtration which hardens the radiation beam. It decreases patient dose while increasing penetration through the patient thus employing lower milliamperes (mA), shorter and steeper pulses. Smaller focal spots are used: therefore, it is possible to obtain

Table 1. Parameters used in fluoroscopy mode for the conventional Xper and Clarity IQ in a clinical cerebral protocol.

Protocol Modality Device	Cerebral Eco Dose 2fps Xper versus Cerebral 2fps Clarity IQ					
	Low		Normal		High	
	Xper	Clarity IQ	Xper	Clarity IQ	Xper	Clarity IQ
kVp	81	83	75	77	71	71
mA	11.7	3.2	11.5	7.0	8.6	6.3
Focal spot size (mm)	0.4	0.4	0.4	0.4	0.4	0.4
Frame length (ms)	6.1	5.0	6.7	5.0	6.3	5.4
Frame per second (fps)	12.5	12.5	12.5	12.5	12.5	12.5
Additional filter	0.9 mm Cu 1 mm Al	0.4 mm Cu 1 mm Al	0.4 mm Cu 1 mm Al	0.4 mm Cu 1 mm Al	0.1 mm Cu 1 mm Al	0.1 mm Cu 1 mm Al
Air Kerma rate (mGy s ⁻¹)	0.10	0.08	0.20	0.13	0.36	0.26

Table 2. Parameters used in cineangiography mode for the conventional Xper and Clarity IQ in a clinical cerebral protocol.

Protocol Device	Cerebral Eco Dose 2fps Xper versus Cerebral 2fps Clarity IQ	
	Xper	Clarity IQ
kVp	80	75
mAs	19	10
Focal spot size (mm)	0.7	0.7
Frame length (ms)	45	45
Frame per second (fps)	2	2
Additional filter	—	0.1 mm Cu 1 mm Al
Air Kerma per image (mGy/ frame)	1.06	0.46

less radiation doses while keeping a similar image quality [14, 17].

2.2. Image acquisition

Fluoroscopy images were acquired using a clinical cerebral protocol at 3 dose levels (low, normal and high); cineangiography images were acquired using a clinical cerebral protocol at normal dose level. Thus, 4 acquisitions were obtained for the conventional Xper technology and 4 acquisitions were taken after the Clarity IQ upgrade, for a total of 8 different image sets.

The parameters used in Xper and Clarity IQ acquisitions are summarized in table 1 for the fluoroscopy modality and in table 2 for the cineangiography modality. Using the external probe of a RaySafeTM x-ray dosimeter (Unfors RaySafe, Sweden) we measured the air kerma rates at the interventional reference point (IRP) and compared them with the ones given by the angiography system. Each acquisition set was repeated three times; to have different nonstochastic noise realizations the phantom was moved of about 1 cm in casual directions once per acquisition. Then, we computed the background variance as a function of frame number and we noted that it stabilized within three frames. In fact, after three frames, the background variance of a specific acquisition protocol does not vary more than 10% among the different frames. Thus, at

least the first 3 images of a series need to be discarded to stabilize the results.

Since the fluoroscopy acquisitions were at 12.5 fps, four series of 10 s were saved. The initial five images of each series (20 overall) were not considered in order to include only the stabilized images in our study. Each image set contains 500 images, discarding the first five images of every series, 480 images remained.

For cineangiography acquisitions we had 2 fps: 27 series of 10 s were saved (total: 540 images). After discarding the first three images of every series, we obtained 459 images.

2.3. Phantom and set-up

A TO10 phantom (Leeds Test Objects, North Yorkshire, UK) was employed in the evaluation of the image quality. The phantom has 108 details available: 12 different diameters (size range: 0.25 mm–11.1 mm), each with 9 different contrasts (declared range: 0.012–0.930 at 70 kVp with 1.00 mm Cu filtration). We used two 10 cm thick homogeneous solid water slabs and we inserted the phantom in the middle at the isocenter. The source to detector distance (SDD) was fixed to 100 cm, the source to isocenter distance was 81 cm. (figure 1). To properly image the phantom, which had a diameter of 18 cm, we used a FOV of 31 cm diagonal. In our acquired images the phantom had a diameter of about 22.1 cm, so the magnification factor was about 1.23.

2.4. Channelized hotelling observer (CHO)

In our work, the decision task was binary: signal present or signal absent. The decision was made by the model observer, determining which of the two classes the data set fell into.

2.4.1. CHO characterization

Following our previous experience [13], we decided to use the CHO to classify images into one of the two mentioned classes. The reason of this choice lies in its capability to reproduce the human observer behaviour, as shown in many previous studies [2, 18–21]. The Hotelling observer is a linear model and it



Figure 1. Picture of the acquisition set-up.

compares a fixed template with the data at every possible signal location. Here, a 2-alternative forced choice (2-AFC) task was used: the model observer (MO) calculated the template output at each of the two locations and chose the one that produced the highest response. The image was processed by a set of channels that were tuned to a given range of spatial frequencies and other parameters. In our study we used Gabor channels profiles. The rationale behind this choice was deeply discussed in our previous work [13]. This channel-set is anthropomorphic and aims to include aspects of the Human Visual Systems (HVS). The number of channels, as well as their central frequencies, orientations and phase factors are parameters that needs to be chosen taking into account the kind of task we want to accomplish. The choice of the central frequencies was also limited by the design of the phantom used in our study (which, in return, allowed us to explore a wide range of different diameter dimensions) and by the acquisition modality.

Four central frequencies in cycles/pixel were used (3/128, 3/64, 3/32, 3/16), each with two phases ($\beta = 0, \pi/2$) and 5 orientations ($\theta = 0, 2\pi/5, 4\pi/5, 6\pi/5, 8\pi/5$). Thus, we have obtained 40 ($5 \times 4 \times 2$) Gabor channels. The choice of many orientations was to make our model more general and applicable to different kinds of details (not necessarily circular). To properly estimate the covariance matrix used in the model template, the minimum number of required images is at least 10 times the number of channels, therefore in our study we selected more than 400 images [2]. The signal absent images were not taken in the close proximity of their respective details because of the configuration of the TO10 phantom. In order to

account for this decision and to correct biases caused by heel effect, usually relevant in this kind of images, the following correction was applied to the pixel values of the signal-present images:

$$x'_{ij} = \frac{x_{ij}}{\mu_{img}} \mu_{background} \quad (1)$$

where x'_{ij} is the pixel value after the correction, x_{ij} is the current pixel value, μ_{img} is the mean of the pixel values of the current image and $\mu_{background}$ is the mean of the respective signal-absent image.

2.4.2. Internal noise

Model observers usually perform better than human observers for simple detection tasks. To correct this behaviour, an internal noise is usually added to the model [12]. Internal noise addition does not affect the linearity of our model.

Human observers can take different decisions even when the same images are involved in repeated tasks. This is caused by the different performance of the visual neuronal system [12, 22]. This human behaviour can be described through an internal noise variable (α), which is added to the CHO response λ_0 , using the following equation:

$$\lambda = \lambda_0 + \alpha\chi \quad (2)$$

where λ is the final decision variable and χ is a random variable which follows a normal distribution with zero means and standard deviation σ , which is given by the square root of the variance of the signal absent class.

This parameter α influences heavily the final performance of the MO and it needs to be tuned properly in order to have accurate predictions from our model. In this work, comparison between human observer performances and CHO results points out that the optimal α value is different between the two modalities of image acquisition (fluoroscopy and cineangiography). In order to properly tune conducting human observer studies. CHO tuning was carried out considering the diameters in the range 0.25–5.6 mm. The α value of the internal noise model was varied until differences under 5% between the human and the CHO results were reached.

2.4.3. Model performance estimation

The other important aspect to define when using MOs is the definition of the metric used to assess its performance in the assigned task, which is called figure of merit (FOM). This value is a formal way to quantify how well a given detection strategy performs a task. In our work, the FOM we have decided to use corresponds to the area under the curve (AUC) of a Receiver-Operating Characteristic (ROC) curve, which is usually computed when dealing with binary classification tasks [23], due to its theoretical meaning. Considering a 2-AFC detection task, AUC values are included in the range 0.5 (pure guessing)—1 (absolute certainty). The AUC for a MO is computed through

the concept of signal-to-noise ratio (SNR). If the decision variables are normally distributed [23] we can use the following equation:

$$AUC = \frac{1}{2} + \frac{1}{2} \operatorname{erf}\left(\frac{SNR}{2}\right) \quad (3)$$

SNR is given in terms of the mean and variance of the model responses λ_i , computed for the two classes:

$$SNR = \frac{\bar{\lambda}_1 - \bar{\lambda}_2}{\sqrt{\frac{\sigma_1^2}{2} + \frac{\sigma_2^2}{2}}} \quad (4)$$

AUC provides also a method to compare human and MO performances: in a 2-AFC, AUC can be interpreted as the percentage of correct responses made by the human observer.

The training process employed in our study is called ‘infinite-trained model’ provided by Wunderlich *et al* [24]: this means a testing subset is not used and all the images serve the training process. This training process has been proven successful in Wunderlich’s work as long as the number of training images was more than 300 [24]. The images we acquired were enough to apply the above-described method.

2.4.4. CHO realization

The spatial-domain CHO model and the channel profiles were developed in a MATLAB environment, using the software employed in our previous work. Our image sizes followed the suggestions pointed out by Ferrero *et al* [25] in their study: with our data, the minimum region of interest (ROI) size was 15×15 pixel. The interested reader can refer to our previous work [13] for the mathematical details and the software operational features. Using an Intel Xeon CPU 2.67 GHz, RAM 24 Gb our software takes about three minutes to evaluate all the diameters.

In order to compare all the different AUC curves from every detail diameter, we decided to summarize our results using contrast-detail curves. Contrast-detail curves are an indication of how much contrast a certain system needs, in order to be able to detect a detail of a given dimension. In this study, we computed those plots using the AUC graphs obtained from the CHO; these graphs were fitted using a psychometric function in order to model the behaviour of the eye. Then, the contrast value associated with an AUC of 0.75 was registered and plotted in a graph with its respective object diameter, thus obtaining the contrast-detail curve. The visibility threshold of 0.75 was chosen to set the experiment in the middle between random guess ($AUC = 0.5$) and certain detection of the detail ($AUC = 1$). The main reason of this choice was that in a low contrast detectability task a target (low contrast detail) could be visible only in some frames or images of a sequence due to noise properties of the imaging equipment. If a low contrast is visible 3 times out of 4, it is likely that the equipment is able to reproduce it.

2.5. Characterization of the angiographic equipment

We used our validated model to investigate the performances of a clinical cerebral protocol in different acquisition conditions. Using a Wilcoxon rank-sum test, we have evaluated the possible differences between the modalities cineangiography and fluoroscopy for the two systems (Xper versus Clarity IQ).

3. Results

3.1. Internal noise calibration

The optimal α value for the fluoroscopy modalities (high, normal and low) was 25. Instead, for the cineangiography modality the α value we found is 35. Those α values were not changed for Xper and Clarity IQ technologies in order to properly compare their respective performances in the mentioned tasks.

3.2. Characterization of the angiography systems

The values measured using the external probe camera and those calculated by the angiography systems were in agreement within 5%. To obtain the dose rate from the air kerma rate measured we used the backscatter factor of 1.35. The obtained value was employed for the dosimetric characterization of our experiments as proposed in the European Guidelines for conventional radiography [26]. In table 3, we showed the dose rate values estimated at IRP before and after Clarity IQ installation and the percentage of dose reduction.

As reported in previous studies [14–17, 27–29], the results obtained suggest that the NRT technology reduces the dose in all the investigated modalities with a more evident decreasing in cineangiography.

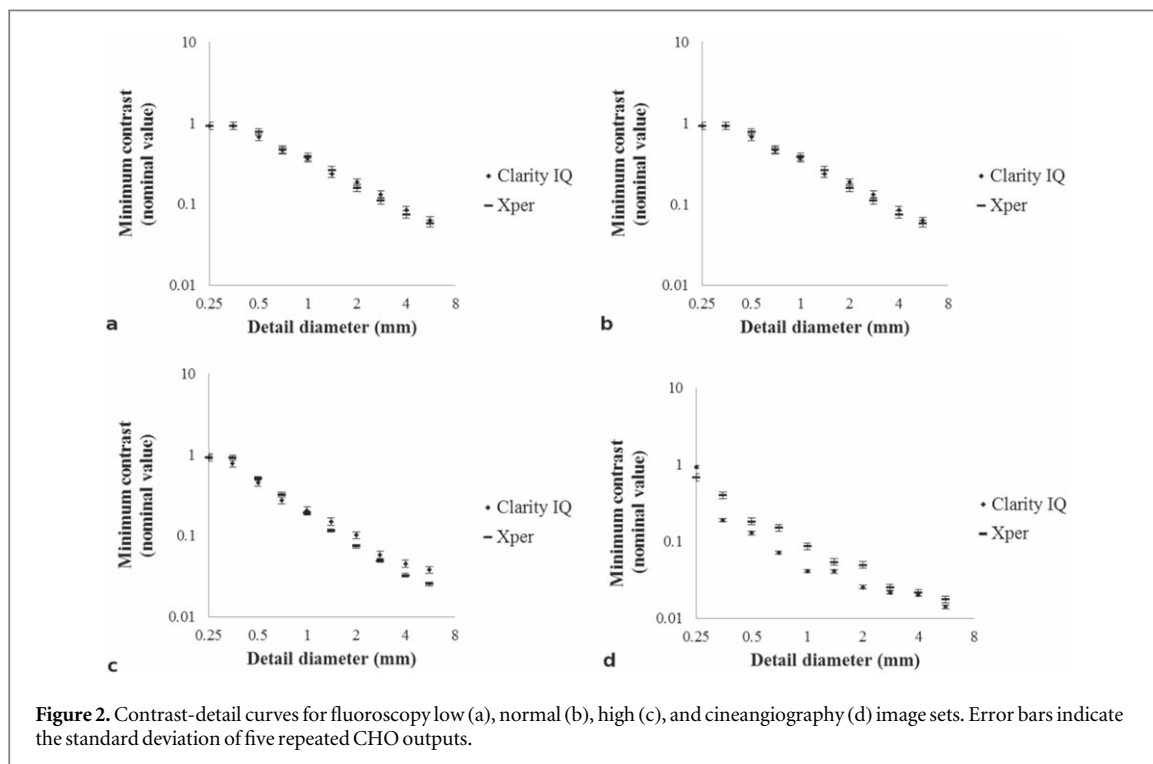
The contrast-detail curves for both systems (Xper and Clarity IQ) associated to fluoroscopy low, normal, high and cineangiography (figure 2) modalities are shown.

On the x -axis the nominal diameters of the details (in mm) are reported, while on the y -axis there is the minimum detectable contrast value, i.e. the contrast value where $AUC = 0.75$. Both axis scales are logarithmic. The error bars associated to the CHO are reported. Those were calculated using one standard deviation of repeated CHO outputs (five times).

Wilcoxon rank-sum test was performed in order to assess the possible differences between our examined imaging settings. Our results are shown in table 4, with p -values associated to their respective modality. These tests confirm there is not a significant difference between contrast-detail curves in fluoroscopy images for all modalities and for cineangiography, even if the dose rates are reduced after Clarity IQ installation.

Table 3. The estimated dose per image and dose rates in the Xper and Clarity IQ systems for each fluoroscopy modalities and cineangiography.

Modality	Xper	Clarity IQ	Reduction (%)
Fluoroscopy low (mGy s^{-1})	0.14	0.11	20%
Fluoroscopy normal (mGy s^{-1})	0.27	0.18	35%
Fluoroscopy High (mGy s^{-1})	0.49	0.35	28%
Cineangiography (mGy/frame)	1.43	0.62	57%

**Figure 2.** Contrast-detail curves for fluoroscopy low (a), normal (b), high (c), and cineangiography (d) image sets. Error bars indicate the standard deviation of five repeated CHO outputs.**Table 4.** p-values associated to the Wilcoxon tests performed on the experiments.

Modality	Xper versus clarity IQ
Fluoroscopy Low	0.910
Fluoroscopy Normal	0.547
Fluoroscopy high	0.164
Cineangiography	0.084

4. Discussion

The aim of this study was to evaluate the impact of a reduction noise technology, Clarity IQ, on radiation doses and static image quality.

NRT can help also in Digital Subtraction Angiography (DSA) because it performs a real-time automatic pixel shift. In this way, there is no motion between the live image and the mask, so the structure noise anatomic can be avoided in the DSA image.

It should be noticed that we started from optimized protocols named ‘Eco Dose’ with our Xper system. Despite this, we found a dose reduction ranging from 20% to 57% in the cerebral protocols after the Clarity IQ upgrade. It is worth noting that the largest dose reduction in fluoroscopy was measured for the

normal dose level compared to the low and high levels. This could mean that the latter two dose levels were more optimized in the previous Xper installment.

These amounts of dose sparing are similar to those already presented in literature, in fact ten Cate *et al* [27] reported that in coronary angiography dose can be reduced by 53% using NRT. Kastrati *et al* [15] described a decrease of dose area product in coronary angiography of 65% and 69% in diagnostic and interventional procedures respectively.

According to Ryckx *et al* [28] the air kerma reduction ranges from 25.5% to 84.4%, Kumashiro *et al* [16] declared a dose reduction of 40% for percutaneous coronary. In addition, in digital subtraction angiography performed in interventional neuroradiology, Soderman *et al* [14] found that patient entrance dose can be reduced by 75% with Clarity IQ. Furthermore, Soderman *et al* [17] analysed interventional neuroprocedures and they reported a dose decreasing of 60%. Eventually, in paediatric cardiac catheterization the dose area product can be reduced by 57.5%, according to Sullivan *et al* [29].

In the previously cited papers the dose reduction was obtained without loss in image quality that was

evaluated with a subjective assessment performed by human observers.

However, human observer studies are time-consuming, costly and suffer significantly from inter- and intra-observer variability. The use of mathematical models in image quality assessment allows us to overcome these limitations. In this paper, we have evaluated the static image quality between the traditional and upgraded systems through a previously validated CHO in terms of low-contrast detectability using a TO10 phantom.

The main limitation of our model is that it considers a simple detection task, i.e. detecting a known circular object placed on a uniform background (SKE/BKE task). Nevertheless, an angiography system usually detects tubular vessels, which cannot be properly modelled using only simple disks. Besides, patient anatomy is not a homogeneous background. Other limitations of this study are that the contrast values are not expressed in iodine concentrations and there is no movement simulation of signal, which is static. For this reasons, the image quality improvement expected with Clarity IQ introduction due to temporal and spatial filtering cannot be fully evaluated with this phantom.

Finally, a low central frequency limited the minimum required dimensions of the sub-ROIs to analyse, while a higher frequency corresponds to a detail too small to give a significant amount of detectable signal for the acquisition system.

Despite these limitations, it has been verified using contrast-detail curves that, for both systems, image quality increases when the dose increases, e.g. from low to high fluoroscopy and the best performance is obtained with cineangiography images.

Moreover, the contrast-detail curves obtained with our CHO model do not present any significant differences between the two analysed systems (Xper and Clarity IQ) for every fluoroscopic and cineangiography modality acquisitions.

From this latter result, we can confirm that the Clarity IQ installation allows to maintain the same overall image quality, while decreasing the delivered dose for our particular task.

The radiation dose reduction is an important factor for patient exposure in order to avoid skin injuries that can occur in protracted x-ray guided procedures. Furthermore, it is crucial for operator radiation protection: a patient dose reduction implies an immediate exposure reduction also for the whole staff involved in the procedure.

5. Conclusion

In conclusion, this study evaluated the impact of a novel noise reduction technology, Clarity IQ, on radiation doses and image quality.

A previously validated CHO model was used to assess the detectability of disk objects within a wide range of diameter sizes and contrasts before and after the Clarity IQ installation.

Our images were acquired using a clinical cerebral protocol with different dose modalities (fluoroscopy low, normal, high and cineangiography) on both configurations (Xper and Clarity IQ).

After tuning the CHO model using human responses, two different internal noise parameters for fluoroscopy and cineangiography were employed. We showed that the model observer did not detect any significant differences in contrast-detail curves before and after the Clarity IQ introduction.

The results suggest that the upgraded Clarity IQ system provides a non inferior image quality compared with the conventional system with an average of 28% and 57% patient dose reduction in fluoroscopy and cineangiography respectively.

Therefore, within the limitations of our study, we can conclude that the Clarity IQ installation has brought a considerable improvement in terms of patient and staff radioprotection.

Acknowledgments

The authors would like to thank Annalisa Terroni for the technical assistance.

ORCID iDs

O Ortenzia  <https://orcid.org/0000-0002-8772-6941>

M Bertolini  <https://orcid.org/0000-0003-3148-1022>

References

- [1] Barrett H H and Myers K J 2004 *Foundations of Image Science* (Hoboken (NJ): Wiley-Interscience)
- [2] Favazza C, Fetterly K A, Hangiandreou N J, Leng S and Schueler B A 2015 Implementation of a channelized hotelling observer model to assess image quality of x-ray angiography systems *Journal of Medical Imaging* **2** 015503
- [3] Yao J and Barrett H H 1992 Predicting human performance by a channelized Hotelling observer model *Mathematical Methods of Medical Imaging* **1768** 23–30
- [4] Yao J and Barrett H H 1992 Predicting human performance by a channelized hotelling observer model *Proc. SPIE* **1768** 161–8
- [5] Wollenweber S D, Tsui B M W, Lalush D S, Frey E C, Lacroix K J and Gullberg G T 1998 Comparison of radially-symmetric versus oriented channel models using channelized hotelling observers for myocardial defect detection in parallel-hole SPECT *IEEE Nuclear Science Symp. and Medical Imaging Conf.* 2090–4 (Cat. No. 98CH36255)
- [6] Abbey C K and Barrett H H 2001 Human- and model-observer performance in ramp-spectrum noise: effects of regularization and object variability *Journal of the Optical Society of America* **18** 473–88
- [7] Lartizen C, Kinahan P E and Comtat C 2004 Volumetric model and human observer comparisons of tumor detection for whole-body positron emission tomography *Academic Radiology* **11** 637–48

- [8] Shidahara M *et al* 2006 Predicting human performance by channelized hotelling observer in discriminating between Alzheimer's dementia and controls using statistically processed brain perfusion SPECT *Annals of Nuclear Medicine* **20** 605–13
- [9] Park S, Gallas B D, Badano A, Petrick N A and Myers K J 2007 Efficiency of the human observer for detecting a Gaussian signal at a known location in non-Gaussian distributed lumpy backgrounds *Journal of the Optical Society of America a-Optics Image Science and Vision* **24** 911–21
- [10] Burgess A E and Colborne B 1988 Visual signal-detection. 4. Observer inconsistency *Journal of the Optical Society of America a-Optics Image Science and Vision* **5** 617–27
- [11] Lu Z L and Doshier B A 1999 Characterizing human perceptual inefficiencies with equivalent internal noise *Journal of the Optical Society of America a-Optics Image Science and Vision* **16** 764–78
- [12] Zhang Y, Pham B T and Eckstein M P 2007 Evaluation of internal noise methods for Hotelling observer models *Med. Phys.* **34** 3312–22
- [13] Bertolini M, Trojani V, Nitrosi A, Iori M, Sassatelli R, Ortenzia O and Ghetti C 2019 Characterization of GE discovery IGS 740 angiography system by means of channelized hotelling observer (CHO) *Phys. Med. Biol.* **64** 095002
- [14] Söderman M, Holmin S, Andersson T, Palmgren C, Babic D and Hoornaert B 2013 Image noise reduction algorithm for digital subtraction angiography: clinical results *Radiology* **269** 553–60
- [15] Kastrati M, Langenbrink L, Piatkowski M, Michaelsen J, Reimann D and Hoffmann R 2016 Reducing radiation dose in coronary angiography and angioplasty using image noise reduction technology *Am. J. Cardiol* **118** 353–6
- [16] Kumashiro M, Kataoka T, Yokota S, Nakagawa S, Otsuki K, Miyake N, Osumi S and Yamaoka K 2018 Image quality of the coronary angiography with noise reduction technology to decrease the radiation dose *Acta Med. Okayama* **72** 153–64
- [17] Söderman M, Mauti M, Boon S, Omar A, Marteinsdottir M, Andersson T, Holmin S and Hoornaert B 2013 Radiation dose in neuroangiography using image noise reduction technology: a population study based on 614 patients *Neuroradiology* **55** 1365–72
- [18] Baydush A H, Catarious D M, Abbey C K and Floyd C E 2003 Computer aided detection of masses in mammography using subregion hotelling observer *Med. Phys.* **30** 1781–7
- [19] Baydush A H, Catarious D M Jr, Lo J Y, Abbey C K and Floyd C E Jr 2001 Computerized classification of suspicious regions in chest radiographs using subregion hotelling observers *Med. Phys.* **28** 2403–9
- [20] Liu H, Chakrabarti K, Kaczmarek R V, Benevides L, Gu S and Kyprianou I S 2014 Evaluation of clinical full field digital mammography with the task specific system-model-based fourier hotelling observer *Med. Phys.* **41** 051907
- [21] Noferini L, Taddeucci A, Bartolini M, Bruschi A and Menchi I 2019 CT image quality assessment by a channelized hotelling observer (CHO): application to protocol optimization *Physica Medica* **32** 1717–23
- [22] Lu Z L and Doshier B A 1999 Characterizing human perceptual inefficiencies with equivalent internal noise *J. Opt. Soc. Am. A* **16** 767–78
- [23] Wunderlich A and Noo F 2009 Estimation of channelized hotelling observer performance with known class means or know difference of class means *IEEE Trans. Med. Imaging* **28** 1198–207
- [24] Wunderlich A, Noo F, Gallas B D and Heilbrun M E 2015 Exact confidence intervals for channelized hotelling observer performance in image quality systems *IEEE Trans Med. Imaging* **34** 453–64
- [25] Ferrero A and Favazza C 2017 Practical implementation of channelized hotelling observers: effect of ROI size *Proc. SPIE Int. Soc. Opt. Eng* **10132**
- [26] European Commission 1996 *European Guidelines on Quality Criteria for Diagnostic RADIOGRAPHIC images* (Brussels: EUR 16260 EN)
- [27] ten Cate T, van Wely M, Gehlmann H, Mauti M, Camaro C, Reifart N, Suryapranata H and de Boer M J 2015 Novel X-ray image noise reduction technology reduces patient radiation dose while maintaining image quality in coronary angiography *Neth Heart J* **23** 525–30
- [28] Ryckx N, Sans-Merce M, Meuli R, Zerlauth J B and Verdun F R 2016 System upgrade on Philips Allura FD20 angiography systems: effects on patient skin dose and static image quality *Radiat Prot Dosim* **169** 313–8
- [29] Sullivan P M, Harrison D, Badran S, Takao C M and Ing F F 2017 Reduction in radiation dose in a pediatric cardiac catheterization lab using the Philips AlluraClarity x-ray system *Pediatr Cardiol* **38** 1583–91